Journal of Engineering Mechanics and Machinery (2026)
Clausius Scientific Press, Canada

DOI: 10.23977/jemm.2026.110105
ISSN 2371-9133 Vol. 11 Num. 1

Numerical Simulation of Capillary Performance in Sintered Copper-Powder Wicks and Optimization of Segmented Structures

Kun Sun

University of Shanghai for Science and Technology, Shanghai, China

Keywords: Heat Pipe, Sintered Copper Powder Wick, Capillary Pressure, Particle Size, Segmented Particle Size Structure

Abstract: The capillary pressure and permeability of a wick jointly determine the liquid return capability and the heat transfer limit of heat pipes. In this work, a numerical model for spontaneous imbibition is developed by coupling phase transport in porous media, Darcy flow, and the Brooks-Corey relationships. Transient simulations are conducted for wicks with five particle sizes under two porosity conditions (ε), to evaluate the capillary performance and to propose a segmented particle-size enhancement strategy. The results show that, at ε = 26%, the wick performance increases monotonically with particle size. In contrast, at ε = 47%, the performance first increases and then decreases with particle size. A segmented design with particle sizes of 600 + 400 μm is therefore proposed, which improves the average mass flow rate and the average capillary rise velocity by 44.6% and 25.6%, respectively, compared with the best uniform particle-size case. The segmented configuration improves the early-stage liquid supply while maintaining a relatively high capillary head, thereby enhancing the overall capillary performance of the wick. These findings provide useful guidance for structural optimization and design of heat pipe wicks.

1. Introduction

Heat pipes are among the most effective passive thermal management devices and have been extensively deployed in electronics, spacecraft, and high performance computing systems [1-3]. Their heat-transport capability is strongly governed by the wick, which must simultaneously provide sufficient capillary driving pressure for liquid return and adequate permeability to minimize flow resistance. For metallic wicks, however, these requirements are intrinsically competing: reducing pore size increases capillary pressure but typically penalizes permeability, whereas enlarging pores improves permeability at the expense of capillary head [4-7]. This trade-off remains a central bottleneck for pushing heat pipes and vapor chambers toward higher heat-flux operation.

Sintered copper powder wicks have long served as a mainstream option due to their robust capillary performance and the broad tunability of pore characteristics through particle size, morphology, and packing/sintering conditions. Hoan et al. [8] compared porosity and capillary behavior of sintered copper-powder wicks with different particle sizes and shapes, showing an overall improvement in capillary performance with increasing particle size and demonstrating that dendritic

powders can achieve higher porosity and enhanced capillary efficiency. Complementary evidence has been reported for other sintered metallic wicks; for example, Zhang et al. [9] highlighted the decisive role of pore architecture in capillary pumping through systematic characterization of sintered stainless steel powder wicks. To overcome the capillary-permeability compromise at the structural level, Byon and Kim [10] proposed bi-porous copper wicks in which large pores serve as low resistance return pathways while small pores sustain high capillary pressure. Similarly, Li et al. [11] introduced multiscale microgrooved features into sintered copper-powder wicks to synergistically enhance liquid transport by combining capillary pumping with improved flow channel capacity. Alongside these experimental advances, modeling efforts have progressed to better describe capillary imbibition in porous media. Alaamri et al. [12] showed that multilayer porous systems can exhibit nontrivial resistance partitioning and distinct wetting-front evolution. Cheng et al. [13] further developed a fractal capillary bundle framework to infer relative permeability from capillary pressure, offering a pathway toward more physically consistent constitutive relations in complex pore structures.

Despite these contributions, a practical and optimization-oriented numerical route that coherently links particle size and pore scale attributes to macroscopic imbibition dynamics-thereby enabling systematic parametric design-remains insufficiently established for sintered copper powder wicks. In this study, we develop a transient numerical model for spontaneous imbibition by coupling phase transport in porous media, Darcy flow, and the Brooks-Corey formulation [14]. On this basis, we quantify the capillary performance of sintered copper powder wicks across particle sizes under different porosities and further propose a segmented particle size architecture to alleviate the early stage supply limitation while maintaining a high capillary head. The presented framework provides reusable methodological support for wick design and structural optimization in high heat flux heat pipes and vapor chambers.

2. Model Development

2.1 Physical Model

This study focuses on the open capillary rise process in a sintered copper powder wick. To be consistent with the experimental conditions, a two dimensional computational domain is constructed, as schematically illustrated in Fig 1. The wick is represented by a rectangular porous medium region whose bottom boundary is in contact with a liquid reservoir. The region above the advancing liquid front is occupied by the gas phase. Driven by capillary pressure, the liquid rises through the pore space within the porous matrix, forming a moving wetting front.

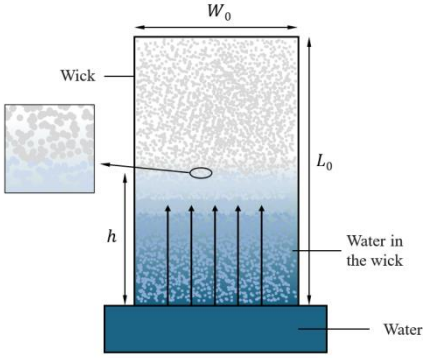

Figure 1. Schematic diagram of the numerical simulation capillary rising model

The porosity of the porous wick,ε, is defined as the ratio of the pore volume to the total volume:

$$\varepsilon = 1 - \frac{V_s}{V} \tag{1}$$

where V is the total volume and V_s is the volume of the copper powder.

In this work, the sintered copper powder is idealized as monodisperse spherical particles with a uniform radius. Figure 2 illustrates the two ideal packing configurations considered in this study, which are used to determine the porosity, permeability, and characteristic pore radius of the sintered porous medium [15]. Figures 2a and 2c correspond to simple cubic (SC) packing. In this configuration, the porosity is $\varepsilon \approx 47\%$, and the characteristic pore radius is given by:

$$Rc = 0.205\, d_s \tag{2}$$

Figures 2b and 2d correspond to hexagonal close packing (HCP). In this configuration, the porosity is $\varepsilon \approx 26\%$, and the characteristic pore radius is given by:

$$Rc = 0.0775\, d_s \tag{3}$$

where d_s denotes the diameter of the copper powder particles.

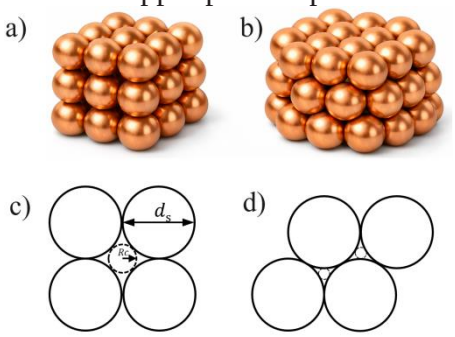

Fig 2. Schematic diagram of particle accumulation method: a) simple cubic arrangement and stacking; b) Dense accumulation of six parties; c) Simple cubic stacked aperture diagram; d) Hexagonal dense stacking pore size diagram

The permeability of the wick, K, is calculated using the Blake-Kozeny equation [4]:

$$K = \frac{{d_s}^2 \varepsilon^3}{150(1-\varepsilon)^2} \tag{4}$$

In porous media, liquid imbibition is driven by the capillary pressure P_{ec}, which can be evaluated using the Laplace-Young equation [5]:

$$P_{ec} = \frac{2\sigma \cos\theta}{Rc} \tag{5}$$

where σ is the surface tension of the liquid and θ is the contact angle. For oxidized surfaces, the contact angle can reach 80 °or even higher. In the fabrication of sintered copper powder heat pipes, the wick is typically subjected to hydrophilic treatment, θ is set to 30 °in this study [18].

In the numerical simulations, the wick is placed vertically; therefore, the capillary driving force is balanced by viscous resistance along the flow path and gravity. Accordingly, the capillary pressure and the pressure drop satisfy the following relationship:

$$\frac{2\sigma \cos\theta}{Rc} = \frac{\mu\varepsilon}{K} h \frac{dh}{dt} + \rho g h \tag{6}$$

where h is the capillary rise height and g is the gravitational acceleration.

The relationship between the capillary rise height and the imbibed liquid mass, m, is given by:

$$h = \frac{m}{\rho \varepsilon A} \tag{7}$$

If gravity is neglected, the equation reduces to the Washburn equation [8]:

$$h = \sqrt{\frac{2\sigma}{\varepsilon\mu} \cdot \frac{K\cos\theta}{Rc}} \cdot \sqrt{t} \tag{8}$$

By combining Eqs. (7) and (8), we obtain:

$$m = \rho\varepsilon A \cdot \sqrt{\frac{2\sigma}{\varepsilon\mu} \cdot \frac{K\cos\theta}{Rc}} \cdot \sqrt{t} \tag{9}$$

2.2 Mathematical Model

2.2.1 Basic Assumptions

Given the complex microstructure of sintered copper powder wicks, the following assumptions are adopted to ensure numerical tractability while remaining representative of practical operating conditions:

(1) The wick is treated as a macroscopically homogeneous and isotropic porous medium. The contact angle θ, porosity ε, and permeability K are assumed constant for each case.

(2) Both the liquid and gas phases are modeled as incompressible Newtonian fluids. The material properties ρ, μ, and σ are taken as constants at the experimental temperature, and the gas phase is treated as a low density fluid.

(3) The flow velocity is sufficiently low that the Reynolds number is very small. The flow is therefore assumed to strictly follow Darcy's law, and inertial effects are neglected.

2.2.2 Governing Equations

In the pore space of the sintered copper-powder wick, both a wetting phase and a non-wetting phase coexist. The wetting-phase saturation is denoted by S_w, and the non-wetting-phase saturation by S_n, with the constraint $S_w + S_n = 1$.

The mass conservation equation for the two phase flow within the porous medium can be expressed as:

$$\frac{\partial(\varepsilon\rho_i S_i)}{\partial t} + \nabla \cdot (\rho_i u_i) = 0 \tag{10}$$

Where ρ_i is the density of phase i, u_i is the Darcy velocity of phase i, $i = w$、n, and t denotes time.

The momentum transfer for both phases within the porous medium is governed by Darcy's law. The Darcy velocity for phase i is given by:

$$u_i = -\frac{Kk_{r_i}(S_i)}{\mu_i}(\nabla p_i - \rho_i g) \tag{11}$$

where μ_i and ρ_i denote the dynamic viscosity and density of phase i, respectively, ∇p_i is the pressure gradient of phase i, and $k_{r_i}(S_i)$ represents the relative permeability, which is a function of the phase saturation S_i.

To characterize capillarity within the porous medium, the Brooks-Corey model was employed to close the relationship between the capillary pressure and the relative permeabilities.

The effective saturation of the wetting phase is defined as:

$$S_e = \frac{S_w - S_{wr}}{1 - S_{wr} - S_{nr}} \tag{12}$$

where S_{wr} and S_{nr} are the residual saturations of the wetting phase and the non-wetting phase, respectively.

The liquid front capillary pressure P_c is determined by both the wetting phase saturation S_w and the entry capillary pressure P_{ec}. This relationship can be expressed as:

$$P_c = P_{ec} S_e^{\frac{-1}{\lambda p}} \tag{13}$$

where λp is the pore size distribution index, defined as $\lambda p = 3 - D_f$ to characterize the pore-size distribution [13]. Here, $D_f = d - \frac{ln\,\varepsilon}{ln\,\beta}$ is the fractal dimension of the porous medium, where d is the Euclidean dimension (taken as $d = 2$ in this study). β is the ratio of the minimum to maximum pore size and is set to 0.01 [20].

2.3 Boundary Conditions

To ensure consistency between the simulation and the experimental boundary conditions, the wick was modeled as a two dimensional planar domain with a length of L_0 and a width of W_0. The thickness was accounted for via an equivalent parameter t_h. The initial reference pressure for the entire computational domain was set to $P_{ref} = 1\ atm$. The temperature field was solved in terms of relative pressure. The two phase saturation and pore scale seepage were resolved by coupling the "Porous Medium Phase Transfer" model with Darcy's law.

The bottom of the wick was in contact with an external liquid reservoir. This contact was modeled as a boundary with sufficient liquid supply at ambient pressure. Consequently, the relative pressure at the bottom boundary was set to $P_b = 0$, and the liquid saturation was fixed at $S_w = 1$. Furthermore, it was assumed that no gas phase entered the porous medium from the bottom, the gas phase mass flux is set to zero.

At the top, an equivalent pressure boundary condition, which varies with the local saturation, was applied. This condition is defined as $P_t = -P_c$, where P_c is the capillary pressure. The gas phase mass flux at this boundary was specified by Equation (14).The volumetric flux of the liquid phase is set to zero.

$$\boldsymbol{n} \cdot \boldsymbol{J}_n = \rho_n(\boldsymbol{u_n} \cdot \boldsymbol{n}) \tag{14}$$

where $\boldsymbol{n}$ is the outward unit normal vector to the boundary, $\boldsymbol{J}_n$ is the mass diffusion flux of the gas phase, ρ_n is the gas-phase density, and $\boldsymbol{u_n}$ is the Darcy velocity of the gas phase within the porous medium.

Both side boundaries were defined as no flux walls. This condition represents physically adiabatic sidewalls with no mass exchange.

3. Simulation Results and Analysis for the Wick with Uniform Particle Structure

3.1 Data Processing, Grid Independence, and Validation

This study investigated the capillary performance of wicks with five different particle sizes under two porosity conditions. The wick dimensions were set as follows: height L_0 =200 mm, width W_0=10 mm, and thickness t_h=3 mm. Air and water at 20 ℃ were employed as the gas and liquid phases, respectively. The pore radius and permeability of the wick were calculated using Equations (2),(3) and Equation (4), with the results summarized in Table 1. The numerical model was solved transiently using a finite element software. To ensure the accuracy of the model, a grid independence study was conducted. Based on the numerical results obtained with different mesh sizes, a grid of 500×50 elements was selected, as the temporal evolution of the capillary rise height exhibited a difference of less than 0.3% compared to that obtained with a finer 550×55 mesh. A time step of 0.05 s was adopted

for the simulations, with a total duration of 20 s.

Table 1. Structural parameters of the wick

particle size d_s (μm)	Porosity ε (%)	predicted permeability K (m^2)	predicted pore radius Rc (μm)
75	26	1.20362E-12	5.8125
150		4.81446E-12	11.625
400		3.42362E-11	31
500		5.3494E-11	38.75
600		7.70314E-11	46.5
75	47	1.38603E-11	15.375
150		5.54413E-11	30.75
400		3.94249E-10	82
500		6.16014E-10	102.5
600		8.8706E-10	123

To further assess the reliability of the proposed model, the capillary rise height is evaluated under different particle diameters and porosities. The parameters reported in the literature are incorporated into the numerical model, and the predicted results are compared with the corresponding experimental measurements reported in Ref. [10].

To quantitatively evaluate the agreement between the numerical model and the experimental data from the literature, the relative error is defined as:

$$\delta = \frac{|m_{sim} - m_{exp}|}{m_{exp}} \times 100\% \tag{15}$$

where m_{sim} and m_{exp} are the simulated and experimental values of the imbibed liquid mass, respectively.

Figure 3 compares the simulated results with the experimental data and the Washburn-equation fitting for wicks with different specifications. The maximum relative error is 7.8%. Overall, the simulations tend to predict slightly higher imbibed mass than both the experiments and the analytical fitting results. This deviation is mainly attributed to discrepancies between the numerical assumptions and the real operating conditions. In the model, the porous medium is treated as homogeneous, and the effective parameters (e.g., porosity, permeability, and characteristic capillary radius) are assumed spatially uniform, whereas these properties are generally non-uniform in practice. In addition, the boundary conditions and pressure settings are idealized in the simulations, implicitly assuming unobstructed venting of the gas phase. In reality, the complex wick microstructure may trap gas within the pore network, which impedes liquid penetration. Such non-ideal experimental factors are not fully captured in the present model, leading to a slight overprediction. Nevertheless, the simulated and experimental trends agree well and the error remains within an acceptable range, indicating that the proposed model can reasonably represent the capillary imbibition behavior of sintered copper powder wicks and can therefore be used for comparative parametric studies.

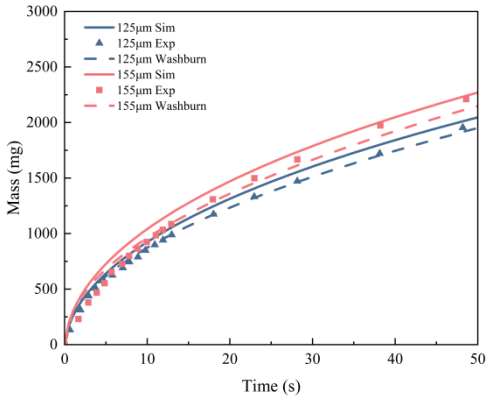

Fig 3. Comparison of simulation results with experimental and Washburn results

3.2 Effects of Porosity and Particle Size on Capillary Rise in the Wick

As shown in Fig 4a, the capillary rise height varies markedly with porosity and particle size. For $\varepsilon = 26\%$, the capillary rise height increases monotonically with particle diameter throughout the entire time window. At t = 20 s, the wick with a particle diameter of 600 μm reaches a capillary rise height of 173.5 mm, which is 146.8% higher than that of the 75 μm case (70.3 mm). Consistent with the capillary rise velocity profiles in Fig 4b, the increasing rise height leads to a progressively larger hydrostatic pressure during the ascent, causing the rise height curves to gradually level off. Notably, the decay in rise velocity is slower for larger particle sizes. This behavior can be attributed to the restricted pore connectivity and limited flow pathways in the low porosity structure, where viscous resistance more readily dominates the imbibition dynamics. Increasing the particle size enlarges the characteristic pore size, reduces flow resistance, and thereby allows the liquid to advance to a higher position within the same time.

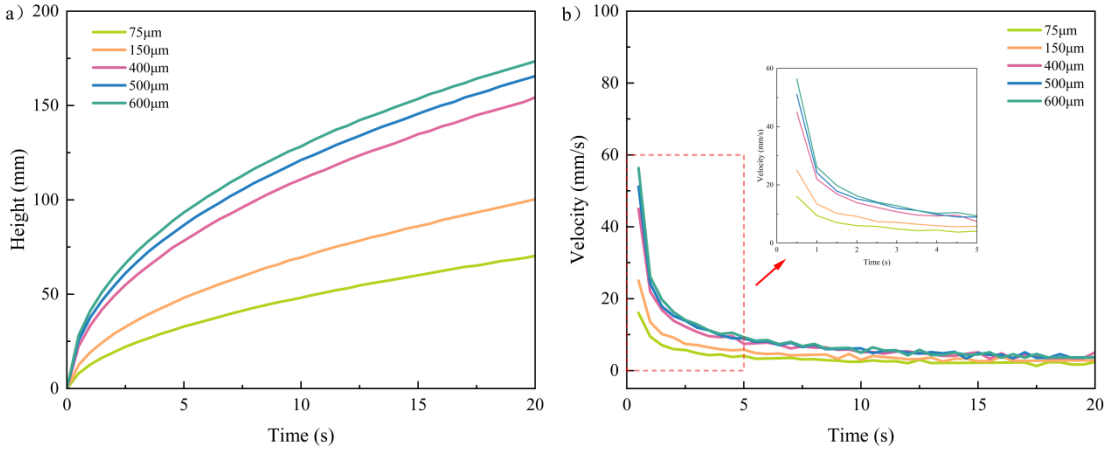

Fig 4. Results at ε=26%: a) Capillary rise height curve; b) Capillary rising velocity curve

Figure 5 shows the results for $\varepsilon = 47\%$. In contrast to the $\varepsilon = 26\%$ cases, the relative ordering of the capillary rise curves changes substantially: increasing particle size does not necessarily lead to a higher rise height, and the rise-height curves for certain particle sizes intersect at later times. During the first 5 s, the 600 μm wick exhibits the largest rise height; however, with increasing time, the 400 μm wick becomes dominant and achieves the highest rise height at t = 20 s, followed by the 500 μm case. Compared with the 400 μm wick, the capillary rise height of the 600 μm wick decreases by 15.9% at t = 20 s.These observations indicate that, in a high porosity structure, the pore network

already provides sufficiently large flow passages, such that the resistance-reduction benefit gained by further increasing particle size becomes marginal. Meanwhile, a larger particle size increases the characteristic pore radius and thus reduces the capillary driving pressure. As a result, at later stages the imbibition process becomes more strongly constrained by the weakened capillary head together with gravity and the associated hydrostatic pressure, ultimately leading to insufficient advancing capability. Therefore, an optimal particle size range exists under high porosity conditions, and an intermediate particle size achieves a more favorable balance between driving force and flow resistance.

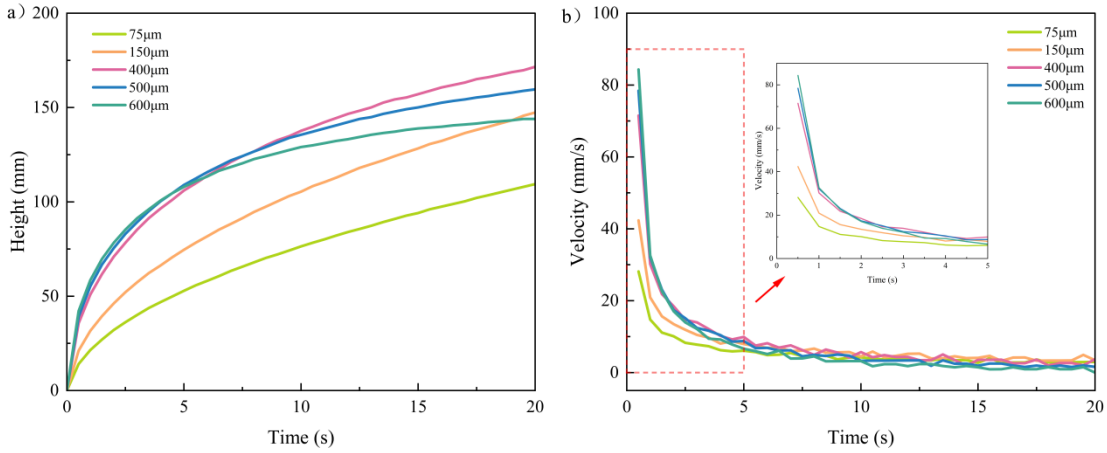

Fig 5. Result plot at ε=47%: a) capillary rise height curve; b) Capillary rising velocity curve

3.3 Effects of Porosity and Particle Size on the Average Mass Flow Rate and Capillary Rise Velocity of the Wick

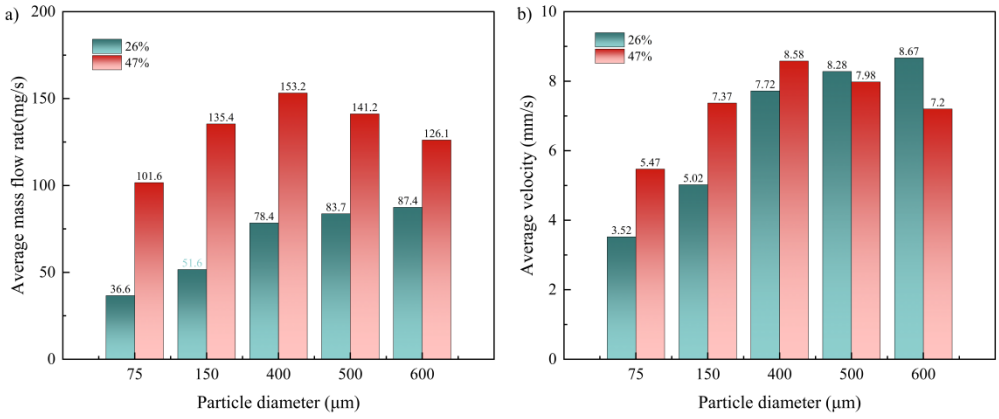

Fig 6. a) Average mass flow rate; b) Average capillary rise velocity

The mean mass flow rate $\bar{m}$ and the mean rise velocity $\bar{v}$ are key metrics for evaluating wick capillary performance, and they affect the maximum heat transport capability of heat pipes [21]. Figure 6 reports the inlet mean mass flow rate and the mean rise velocity of the liquid front over 20 s. When $\varepsilon = 26\%$, both metrics increase monotonically with particle size. The mean mass flow rate rises from 36.6 mg/s to 87.4 mg/s, which corresponds to an increase of 138.8%. Meanwhile, the mean rise velocity increases from 3.52 mm/s to 8.67 mm/s, corresponding to an increase of 146.3%.When $\varepsilon = 47\%$, the average flow rate first increases and then decreases with particle size. As the particle size increases from 75 μm to 400 μm, the mean mass flow rate increases from 101.6 mg/s to 153.2

mg/s, corresponding to an increase of 50.8%; it then decreases to 126.1 mg/s as the particle size further increases to 600 μm. The mean rise velocity shows the same rise then fall trend, increasing from 5.47 mm/s to 8.58 mm/s and then decreasing to 7.2 mm/s. These results again indicate that an optimal particle size of 400 μm exists at high porosity, where high throughput and rapid wetting front advancement are achieved simultaneously. The contrast between the two porosities reflects the role of porosity in balancing capillary driving force against flow resistance.

4. Enhancement of the Capillary Rise Process by the Segmented Particle-Size Wick Structure

As illustrated in Fig 7, during heat pipe operation the wick drives the liquid to return from the condenser to the evaporator. The driving force originates from the capillary pressure difference, whereas the primary resistances arise from the seepage pressure drop through the porous medium and gravity when the return flow is against gravity. In general, the evaporator requires a higher capillary pressure to prevent dry-out, while the condenser benefits more from a higher permeability to reduce the liquid return resistance [22, 23]. Accordingly, this work proposes a segmented wick design in which a high capillary pressure copper powder structure is arranged in the evaporator and a high-permeability structure is arranged in the condenser, thereby balancing capillary driving force and liquid-flow resistance.

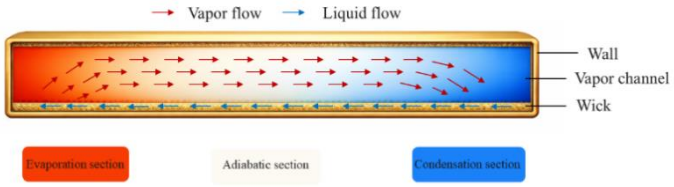

Figure 7. Schematic diagram of the working principle of heat pipes

4.1 Segmented Wick Design

The above results show that, at $\varepsilon = 47\%$, the 600 μm structure exhibits the fastest capillary rise in the early stage, but its rise velocity decreases markedly at later times and rapidly approaches zero. In contrast, when the particle size is 400 μm, the early-stage rise velocity is lower than that of the 600 μm case, yet a relatively high rise velocity can be sustained in the later stage. Motivated by this observation, the following section investigates segmented wick structures as a means to further enhance the capillary performance of the wick.

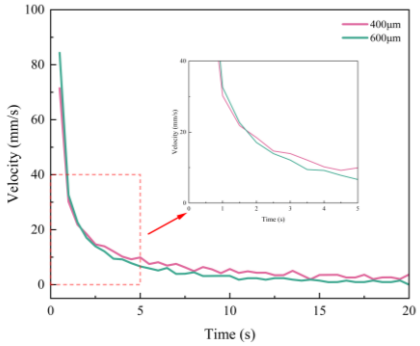

Figure 8. 600 μm and 400 μm particle size wick velocities

Figure 8 shows that the capillary rise velocity curves of the two uniform wicks intersect, indicating a switch in the dominant advantage between the two structures. Therefore, selecting the intersection at which the velocities are equal as the segmentation interface height has clear physical significance.

According to Fig. 8, at t = 2.5 s the velocities satisfy $v_{600} \approx v_{400}$, and the corresponding rise heights are $h_{600} = 85\ mm$ and $h_{400} = 78\ mm$. Based on these results, the segmented wick is designed with $d_s = 600\ \mu m$ in the 0-80 mm region and $d_s = 400\ \mu m$ in the 80-200 mm region, as illustrated in Fig 9. The capillary performance of this segmented particle size wick is then solved and compared with that of uniform particle wicks.

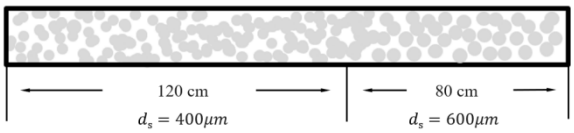

Figure 9. Segmented suction core structure

4.2 Capillary-Performance Enhancement of the Segmented Wick Structure

Figure 10 shows that the segmented wick exhibits a capillary rise height curve that combines rapid initiation with strong late stage performance throughout the process. Figure 10a indicates that the capillary rise height of the segmented wick has already reached its maximum at 15 s; therefore, the capillary rise performance within the first 15 s is analyzed in the following. As shown in Fig 10b, when the liquid front enters the second segment, the capillary rise velocity increases markedly, because the capillary driving force undergoes a step increase at the segment interface.

Consistent with the quantitative results summarized in Table 2, both the mean mass flow rate and the mean rise velocity of the segmented wick are substantially higher than those of the uniform wicks. The segmented design achieves a mean mass flow rate of 266 mg/s, which is 44.6% higher than that of the best uniform wick with a 400 μm particle size, which delivers 184 mg/s. The mean rise velocity reaches 13.15 mm/s, exceeding the best uniform 400 μm case of 10.47 mm/s by 25.6%. These results demonstrate that the segmented particle size wick can improve the early stage liquid supply while maintaining a high capillary head, thereby effectively enhancing the overall capillary performance. Therefore, adopting a segmented wick architecture is a meaningful strategy for structural design and optimization of heat pipe wicks.

Table 2. Comparison of segmented structure and uniform structure

d_s (μm)	$\bar{m}$ (mg/s)	$\bar{v}$ (mm/s)
400	184	10.47
600	157	9.25
600+400	266	13.15

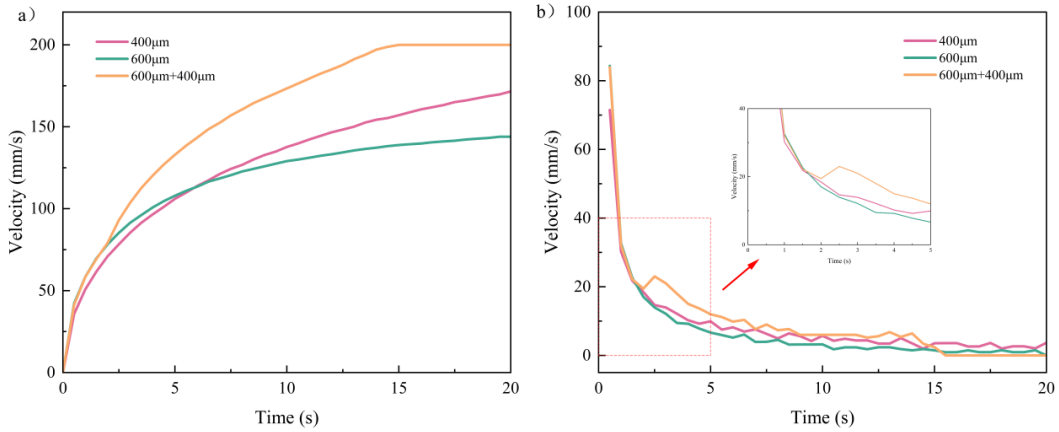

Fig 10. Numerical simulation results of segmented suction core structure: a) capillary rise height curve; b) capillary rising velocity curve;

5. Conclusions

A numerical model for spontaneous imbibition is developed in this study to investigate the capillary-rise behavior of sintered copper-powder wicks under different porosities and particle sizes. The capillary performance is evaluated using metrics including the mean mass flow rate and the mean capillary rise velocity. In addition, a segmented particle size strategy is proposed and examined to enhance the wick performance. The main conclusions are summarized as follows:

(1) At the lower porosity of $\varepsilon = 26\%$, increasing particle size markedly enhances both the capillary rise height and the rise velocity, and the mean mass flow rate and mean capillary rise velocity show the same trend. This indicates that, under low porosity conditions, the imbibition process is more strongly constrained by viscous resistance. The resistance reduction associated with larger particle sizes dominates, whereas the adverse effect of reduced capillary pressure does not become the primary limiting factor within the particle size range investigated in this work.

(2) At the higher porosity of $\varepsilon = 47\%$, an optimal particle size range exists and both the mean mass flow rate and the mean rise velocity exhibit a single peak trend. The inlet mean mass flow rate reaches its maximum at a particle size of 400 μm, and the corresponding mean front velocity also increases first and then decreases, attaining the highest value of 8.58 mm/s at 400 μm. These results indicate that, in high porosity wicks, a competition between permeability gains and capillary pressure decay governs the optimal structural length scale that maximizes the overall liquid return capability.

(3) The segmented particle size design improves the early stage liquid supply while maintaining a high capillary pressure, thereby enhancing the overall liquid return performance. For the 600 + 400 μm segmented configuration, the mean mass flow rate and the mean rise velocity reach 266 mg/s and 13.15 mm/s, respectively, representing increases of 44.6% and 25.6% compared with the best uniform structure. This demonstrates that adopting a segmented wick architecture is a highly effective approach to enhance wick capillary performance and, consequently, improve the thermal performance of heat pipes.

References

[1] Buffone C, Coulloux J, Alonso B, et al. Capillary pressure in graphene oxide nanoporous membranes for enhanced heat transport in Loop Heat Pipes for aeronautics[J]. Experimental Thermal and Fluid Science, 2016, 78: 147–152.

[2] Huang G W, Liu W Y, Luo Y Q, et al. A novel ultra-thin vapor chamber for heat dissipation in ultra-thin portable electronic devices[J]. Applied Thermal Engineering, 2020, 167.

[3] Zhou W J, Li Y, Chen Z S, et al. Ultra-thin flattened heat pipe with a novel band-shape spiral woven mesh wick for cooling smartphones[J]. Int J Heat Mass Transf, 2020, 146.

[4] Bu S, Li H, Yang X, et al. A novel vapor chamber with gradient capillary wick and larger expansion area[J]. Int J Heat Mass Transf, 2025, 246: 127021.

[5] Luo F, Bai J, Yan C, et al. A novel aluminum boss vapor chamber with 3D bioinspired wick for thermal management in electronic chip[J]. Applied Thermal Engineering, 2025, 259: 124853.

[6] Luo J L, Zhao F B, Xu M, et al. Biomimetic Copper Forest Structural Modification Enhances the Capillary Flow Characteristics of the Copper Mesh Wick[J]. Energies, 2023, 16(14).

[7] Yan C M, Li H M, Tang Y, et al. A novel ultra-thin vapor chamber with composite wick for portable electronics cooling[J]. Applied Thermal Engineering, 2023, 226.

[8] Hoan T M, Toan N V, Hung N P, et al. Dependence of Particle Size and Geometry of Copper Powder on the Porosity and Capillary Performance of Sintered Porous Copper Wicks for Heat Pipes[J]. Metals, 2022, 12(10): 1716.

[9] Zhang S, Chen C, Chen G, et al. Capillary performance characterization of porous sintered stainless steel powder wicks for stainless steel heat pipes[J]. International Communications in Heat and Mass Transfer, 2020, 116: 104702.

[10] Byon C, Kim S J. Capillary performance of bi-porous sintered metal wicks[J]. Int J Heat Mass Transf, 2012, 55(15-16): 4096–4103.

[11] Li Q, Lan Z, Chun J, et al. Fabrication and capillary characterization of multi-scale micro-grooved wicks with sintered copper powder[J]. International Communications in Heat and Mass Transfer, 2021, 121: 105123.

[12] Alaamri J, Chandra V, Addassi M, et al. Experimental and numerical investigation of spontaneous imbibition in multilayered porous systems[J]. Energy & Fuels, 2023, 37(16): 11694–11706.

[13] Cheng H, Wang F, Yang G, et al. Prediction of relative permeability from capillary pressure based on the fractal capillary bundle model[J]. Applied Thermal Engineering, 2024, 239: 122093.
[14] Brooks R H, Corey A T. Properties of porous media affecting fluid flow[J]. Journal of the irrigation and drainage division, 1966, 92(2): 61–88.
[15] Tien C, Sun K. Minimum meniscus radius of heat pipe wicking materials[J]. Int J Heat Mass Transf, 1971, 14(11): 1853–1855.
[16] Faghri A. Heat pipe science and technology[M]. Global Digital Press, 1995.
[17] Cassie A, Baxter S. Wettability of porous surfaces[J]. Transactions of the Faraday society, 1944, 40: 546–551.
[18] Sebayang A M S, Tetuko A P, Nurdiyansah L F, et al. Wick parameters (particle size, porosity and contact angle) and performances of a U-shaped heat pipe: experimental, analytical and numerical[J]. Australian Journal of Mechanical Engineering, 2022, 22(3): 552–565.
[19] Washburn E W. The dynamics of capillary flow[J]. Physical review, 1921, 17(3): 273.
[20] Yu B M, Li J H. Some fractal characters of porous media[J]. Fractals-Complex Geometry Patterns and Scaling in Nature and Society, 2001, 9(3): 365–372.
[21] Yin S, Shui Q, Zhao W, et al. Evaluation on capillary performance of multifunctional ultra-thin composite wick[J]. Thermal Science and Engineering Progress, 2024, 51: 102659.
[22] Xia Y, Yao F, Wang M. Experimental Investigation on Thermal Performance of Vapor Chambers with Diffident Wick Structures[J]. Energies, 2023, 16(18).
[23] Yin L, Li J, Wang Z, et al. Experimental study on the heat transfer performance of vapor chamber with uniform/gradient wicks[J]. Case Studies in Thermal Engineering, 2025, 66.